An Integrated Battery Charger With High Power Density and Efficiency for Electric Vehicles

Dong-Hee Kim, *Member, IEEE*, Min-Jung Kim, *Student Member, IEEE*, and Byoung-Kuk Lee, *Senior Member, IEEE*

***Abstract*—Power conversion systems for electric vehicles (EVs) have been researched to improve power density and efficiency at low cost. To satisfy these needs for EVs, this paper proposes a novel battery charging system that integrates a nonisolated on-board charger (OBC) and low-voltage dc–dc converters (LDCs) by sharing the semiconductor devices and mechanical elements. Thus, the volume of LDCs is reduced dramatically compared with a conventional nonintegrated charging system. The proposed integrated system is configured based on a driving condition that is derived from the analysis of vehicle operating modes. In order to improve system's performance, an asynchronous control algorithm is applied to control the OBC optimally. In the LDC system, two *LLC* resonant converters are composed by sharing a transformer and secondary-side components. To increase the efficiency of each LDC, which is operated in the wide input and output voltage range, a duty and frequency control algorithm is proposed. The theoretical analysis, operating strategy, and experimental results on a 6.6-kW OBC and 1.9-kW LDC are presented to evaluate the performance of the proposed system; the total volume of LDCs is 1.87 L, and peak efficiencies of OBC and LDC are 97.3% and 93.13%, respectively. Moreover, a comparative analysis is presented to evaluate the performance of the proposed system.**

***Index Terms*—Control algorithm, electric vehicles (EVs), low-voltage dc–dc converter (LDC), on-board battery charger (OBC), system integration.**

I. Introduction

With an increasing awareness of environmental issues, interest in and research on electric vehicles (EVs) worldwide have increased [1]. In EVs, the battery is a core component that determines the vehicle's performance, and therefore, much research has been carried out to improve EV battery performance. In order to maximize battery performance, power conversion units (PCUs) should also be considered as part of the main technology in EVs. There are four kinds of PCUs connected to the battery: high-voltage dc–dc converters (HDCs), propulsion inverters, on-board chargers (OBCs) for high-voltage batteries (i.e., the propulsion battery), and low-voltage dc–dc converters (LDCs) for auxiliary batteries (12–24 V). Because PCUs are installed in EVs, high efficiency and high power density are the main design considerations, along with cost reduction schemes for mass production. These requirements have led to research on integrated power units.

Previous research on this issue can be summarized as follows. The basic approach for integrating EV PCUs is to use the same housing and cooling system. In the Toyota Prius III, the power density was improved by integrating the reactor with a lower case and the number of components was reduced by integrating connectors [2]. In recent years, some structures to integrate the circuits of the PCU have been proposed. An integrated structure, which integrates the OBC and LDC, was proposed in [3] and [4]. This structure shares a transformer and the secondary side of the isolated OBC with the LDC. This proposed system has the advantages of higher power density and lower cost. However, when the OBC and LDC operate at the same time, the proposed system cannot charge the low-voltage battery or an additional converter is required to regulate the LDC output voltage. Moreover, the efficiency of the LDC operation is low because of the multistage structure. In general, an isolated multistage structure is used in the OBC to satisfy a wide input–output voltage range. In order to increase the system efficiency and the power density, a nonisolated OBCs have been studied by eliminating a transformer, which affects the volume and the efficiency of the system [5]–[9]. These nonisolated OBCs can satisfy SAE J1772, which is the standard of the conductive charger for EVs, because the high-voltage battery (HVB) is floated with the body ground of the vehicle [10]. Also, research of an integrated system based on the nonisolated OBC has been in progress [11]–[18]. An integrated system that uses a motor's inductance and the propulsion as a PFC circuit was studied in [11]–[17]. Another structure, which integrates the OBC and HDC, was proposed in [18]. This structure shares an inductor between the OBC and HDC. However, it has low efficiency because of its structure. As such, the development and research of the integrated charging system, which is based on a high efficiency and low-cost nonisolated OBC, can be considered.

In this paper, a novel concept of an integrated OBC–LDC power unit is proposed to overcome the drawbacks of previous research. The proposed system integrates a nonisolated 6.6-kW OBC and an isolated 1.9-kW high-power LDC (H-LDC) by sharing the electric components and mechanical components of the OBC with the LDC. In addition, an isolated 600-W low-power LDC (L-LDC) is added to operate simultaneously during the charging mode. Although the L-LDC is added, the volume of the integrated power unit does not increase significantly be-

Manuscript received May 19, 2016; revised July 25, 2016; accepted August 15, 2016. Date of publication August 30, 2016; date of current version February 11, 2017. Recommended for publication by Associate Editor M. Ferdowsi.

D. H. Kim is with the Department of Electrical Engineering, Tongmyong University, Busan 48520, Korea (e-mail: mashia@tu.ac.kr).

M. J. Kim and B. K. Lee are with the School of Electronic and Electrical Engineering, Sungkyunkwan University, Suwon-si 16419, Korea (e-mail: kimminjung@skku.edu; bkleeskku@skku.edu).

Color versions of one or more of the figures in this paper are available online at http://ieeexplore.ieee.org.

Digital Object Identifier 10.1109/TPEL.2016.2604404

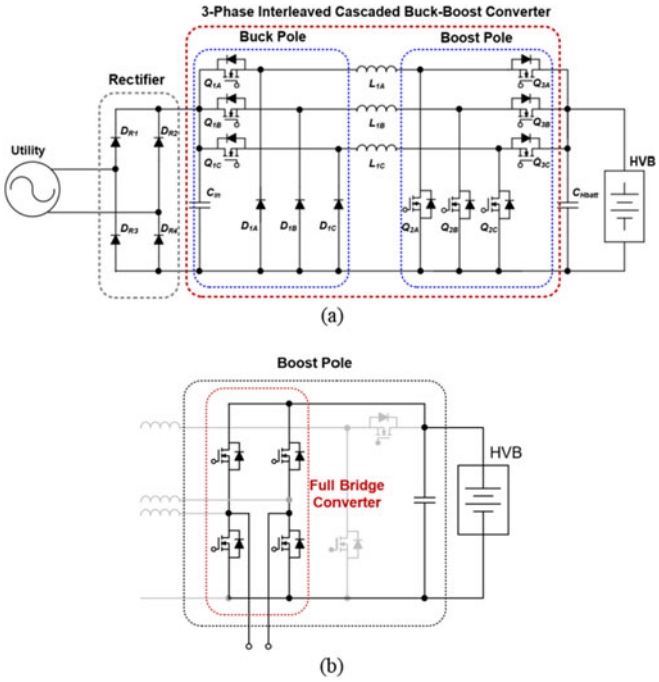

Fig. 1. Nonisolated OBC: (a) three-phase cascaded buck–boost converter and (b) full-bridge structure.

cause the L-LDC shares the transformer and the secondary side with the H-LDC. By sharing the transformer, the design of the two LDC systems is limited by the physical structure of the transformer. In order to overcome this drawback, a duty and frequency control method is adopted in LDC systems. The detailed design and the operating modes of the proposed integrated EV power unit are described, and the validity of the proposed system is verified by informative experimental results, compared with a conventional nonintegrated system. Peak efficiencies OBC and LDC are 97.3% and 93.13%, respectively, and the total volume of LDCs is 1.87 L, which is 83.6% of the LDC of the nonintegrated system.

II. Principles of Proposed Battery Charger

A. Nonisolated OBC and System Integration

The cascaded buck–boost converter is adopted for the nonisolated OBC topology, as shown in Fig. 1(a). The efficiency and the power density of the nonisolated single-stage OBC are much higher than those of the isolated two-stage OBC because of the absence of a transformer and diode rectifier. When the structure of the OBC is designed with a single-phase converter, the discontinuous current flows into the input side of the OBC because of the input buck structure. Therefore, a multiphase structure is needed to make the input-side current continuous [6]. In addition, to charge the HVB at a 6.6-kW power rate, a three-phase cascaded buck–boost converter is used, considering the current rating. The cascaded buck–boost consists of a buck pole, a boost pole, and an inductor. Each switch is controlled according to the input voltage and output voltage relationship. Each phase of the boost pole can be viewed as a full-bridge structure and is connected to the high-voltage battery, as shown in Fig. 1(b). Therefore, two phases of the boost pole can be used as the primary-side switches of the LDC. This structure, however, needs an additional LDC circuit when the OBC and the LDC operate at the same time. The magnitude of current consumption according to electrical load variations in a commercial hybrid car is investigated [19], and the details are summarized in Table I. As shown in Table I, the magnitude of the default electrical load is 25 A, and the full load is 124 A. For this reason, an L-LDC, which shares a transformer with the LDC and the secondary side of the LDC, is added to improve the power density. From the aforementioned concept, the proposed nonisolated integrated OBC–LDC power unit is shown in Fig. 2. The proposed system consists of a nonisolated OBC, H-LDC, and L-LDC. Each LDC adopts an *LLC* resonant network to increase the efficiency and the power density and operate at a wide input and output voltage range; the selecting switch is added to separate the resonant tank of the H-LDC from the OBC.

TABLE I
Current Consumption of LDC According to Electrical Load Variation [19]

Parameter	Current Consumption
Default load	25 A
Light (with taillight) + Head lamp + High beam	25 A
Heating wire (front + back)	15 A
Blower	28 A
Brake light	15 A
Emergency light	9 A
Windshield wipers	7 A
Total	124 A

B. Operating Modes of the Proposed System

The proposed integrated power unit has three operating modes: the OBC standalone mode (Mode I), the LDC standalone mode (Mode II), and the OBC–LDC simultaneous mode (Mode III), as shown in Fig. 3. The detailed description of the operating modes is as follows:

1) *Mode I*: In this mode, only the OBC charges the HVB using the utility grid. The OBC needs to achieve a high power factor (PF) of the input current and should control the output voltage with wide input and output voltage variation. The L-LDC does not operate, and the resonant tank of the H-LDC is separated from the HVB by a switch $Q_{\rm sel}$. The power flow of Mode I is described in Fig. 3(a).
2) *Mode II*: This mode occurs when the OBC does not operate. Thus, H-LDC can charges the low-voltage battery (LVB) with a full-power rate. In order to charge the LVB, four MOSFETs (Q_{2B}, Q_{3B}, Q_{2C}, and Q_{3C}) of the OBC boost pole are used, and $Q_{\rm sel}$ is turned on, as shown in Fig. 3(b).
3) *Mode III*: In this operating mode, the OBC and the L-LDC operate at the same time. The input source is the utility grid, and the loads are the HVB and LVB. Thus, the total

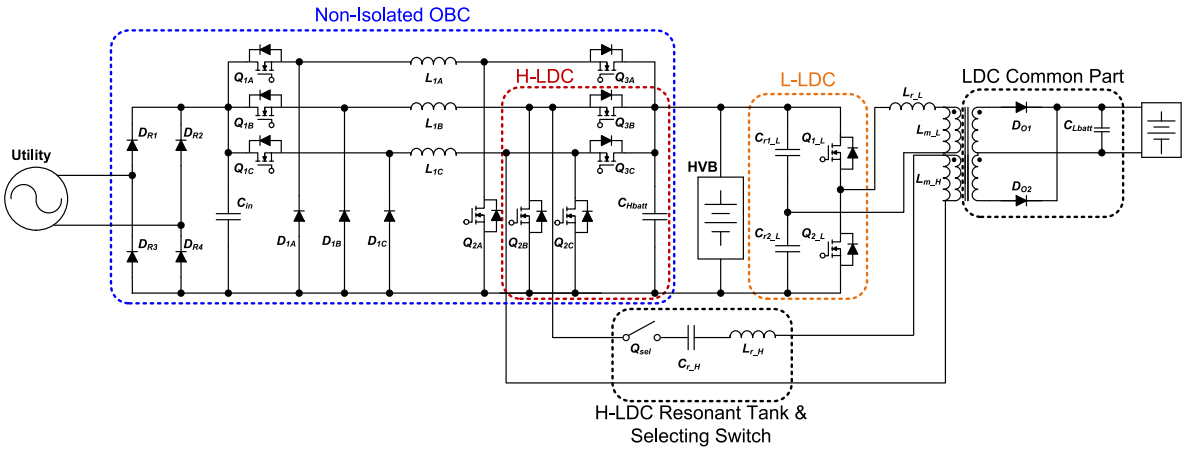

Fig. 2. Configuration of the proposed battery charger.

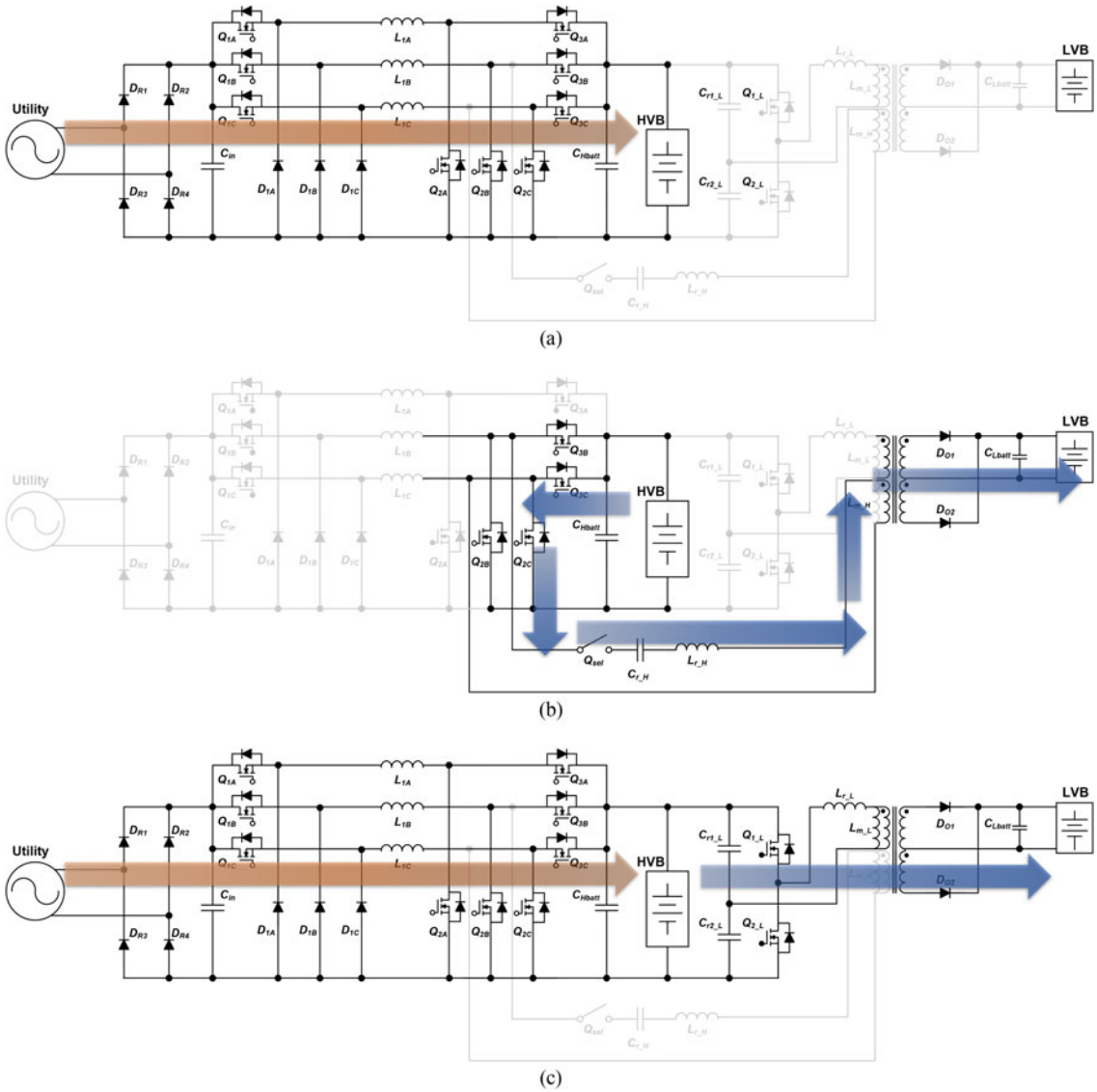

Fig. 3. Operating modes of the proposed system: (a) Mode I, (b) Mode II, and (c) Mode III.

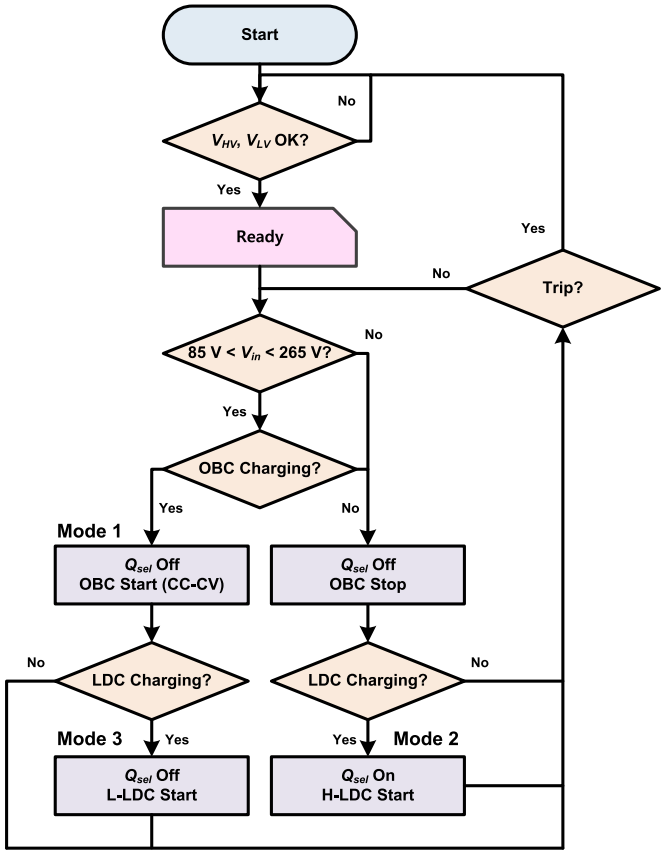

Fig. 4. Flowchart of the mode selection control process.

charging power should not exceed the maximum output of Mode I. If the LVB is fully charged, the operation mode is changed to Mode I. From the half-bridge structure of the L-LDC, the induced transformer voltage is the half of the H-LDC. The power flow of Mode III is shown in Fig. 3(c).

Fig. 4 shows a block diagram of the mode selection control process for the proposed system. First, the system checks the utility grid and status of the batteries. When the OBC charging signal is applied, the proposed integrated power unit operates in Mode I. When the LDC charging signal is added while the integrated power unit operates in Mode I, the integrated power unit changes to Mode III. If the OBC does not operate or the utility grid is not connected, the integrated power unit operates in Mode II, when the LDC charging signal is added.

III. Design Consideration for Proposed Battery Charger

Table II shows system specifications by considering the operating modes and the data in Table I. The maximum output current of the L-LDC is 40 A, and thus, the maximum power of the OBC for Mode III is approximately 6 kW. The frequency of each LDC is limited to 150 kHz because conduction EMI testing of ac/dc applications starts at 150 kHz [20].

TABLE II
System Specifications

	Parameter	Value
OBC	Input voltage	85−265 V_{ac}
	Charging voltage	260−430 V_{dc}
	Charging power	6.6 kW
H-LDC and L-LDC	Input voltage	260−430 V_{dc}
	Charging voltage	12.5−14.5 V_{dc}
	Maximum output current (H-LDC/L-LDC)	130/40 A
	Maximum switching frequency	150 kHz

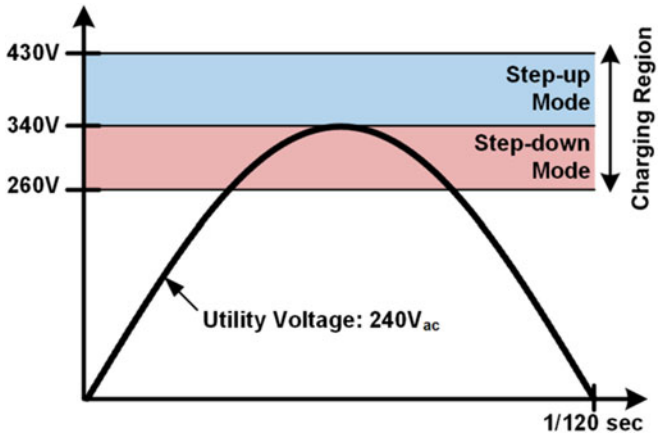

Fig. 5. Operating mode of the nonisolated OBC.

A. Control Strategy of the Nonisolated OBC

As mentioned previously, the OBC and LDCs of the integrated power unit are operated independently or simultaneously; therefore, an optimal design is required to achieve, respectively, high efficiency and power density. The conventional control algorithm of the nonisolated OBC is operated depending on the voltage conditions of the input utility and the output battery, and the OBC operates in two modes: step down and step up, as shown in Fig. 5. In the step-up mode, high efficiency is achieved by controlling only the boost pole switches. However, in the step-down mode, the switching operation of the buck switch and the boost switch occur simultaneously. In the simultaneous switching method, efficiency can be reduced in the buck-mode operation because the current stress of the device increases. To resolve this problem, an asymmetric control algorithm is applied to the cascaded buck–boost converter [8].

The asymmetric control algorithm is a method that generates individual pulsewidth modulation (PWM) signals of the buck switch and the boost switch to regulate the output voltage, as shown in Fig. 6. The input–output voltage gain can be expressed as

$$\frac{V_{o.H}}{|V_{\rm in}|} = \frac{D_{\rm Buck}}{1 - D_{\rm Boost}} \tag{1}$$

where $V_{\rm in}$, $V_{o.H}$, $D_{\rm Buck}$, and $D_{\rm Boost}$ are the input voltage, the HVB voltage, the buck pole switch duty, and the boost pole

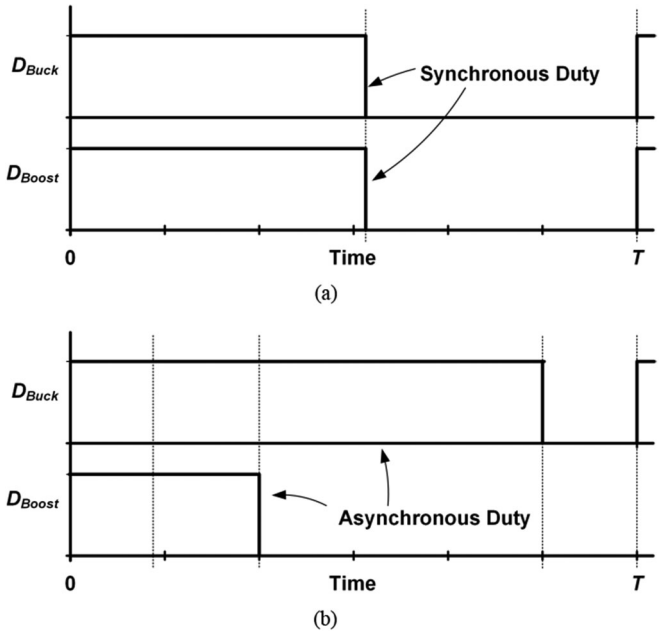

Fig. 6. PWM strategy of the control algorithm: (a) conventional and (b) asynchronous.

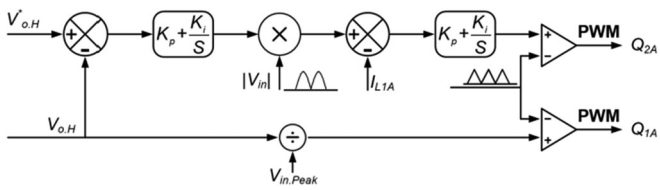

Fig. 7. Controller of the nonisolated OBC for a single phase.

switch duty, respectively. From the asynchronous operation, D_{Buck} can be controlled with a large width compared with the conventional algorithm. The inductor current ripple can be expressed as

$$\Delta I_L = \begin{cases} \dfrac{V_{o.H} \cdot (1 - D_{\mathrm{Buck}})}{L \cdot f_{\mathrm{sw}}} & (V_{\mathrm{in}} > V_{\mathrm{battery}}) \\ \dfrac{|V_{\mathrm{in}}| \cdot D_{\mathrm{Boost}}}{L \cdot f_{\mathrm{sw}}} & (V_{\mathrm{in}} < V_{\mathrm{battery}}) \end{cases}. \quad (2)$$

Fig. 7 shows the control block diagram for the nonisolated OBC based on the asynchronous algorithm to control the input current PF and the charging voltage. In order to reduce the input voltage of the boost pole below the output charging voltage, the buck switch is controlled as

$$D_{\mathrm{Buck}} = \frac{V_{o.H}}{V_{\mathrm{in.peak}}}. \quad (3)$$

D_{Buck} is 1 when the peak input voltage $V_{\mathrm{in.peak}}$ is equal to the output charging voltage. Thus, the mode change from the step-down mode to the step-up mode occurs smoothly. The parameters related to the inductor current for the output charging voltage $V_{o.H}$ values and the corresponding D_{Buck} values are

TABLE III
PARAMETERS OF INDUCTOR CURRENT FOR EACH CONTROL METHOD

	Conventional		Asynchronous	
	$D_{\mathrm{Buck.avg}}$	I_L	$D_{\mathrm{Buck.avg}}$	I_{L}
$V_{o.H}$ = 260 V	0.56	$1.76 \cdot I_{\mathrm{in}}$	0.83	$1.20 \cdot I_{\mathrm{in}}$
$V_{o.H}$ = 311 V	0.61	$1.64 \cdot I_{\mathrm{in}}$	1.00	$1.00 \cdot I_{\mathrm{in}}$

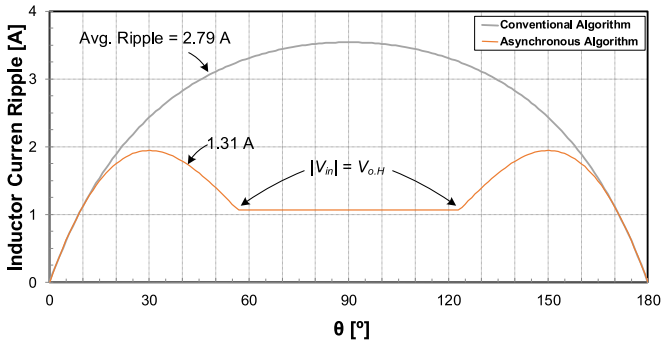

Fig. 8. Inductor current ripple for each control algorithm.

shown in Table III, where $D_{\mathrm{Buck.avg}}$ is the average value of the buck duty. The average inductor current I_{L} can be calculated as

$$I_L = \frac{I_{\mathrm{in}}}{D_{\mathrm{Buck}}}. \quad (4)$$

Because of the reduced inductor current compared with the conventional algorithm, the conduction loss is decreased. Therefore, the efficiency at the step-down mode can be increased by the asynchronous algorithm.

B. Inductor Design of the Nonisolated OBC

In order to design the inductor of the OBC, the stored energy and current ripple of the inductor should be analyzed. The stored energy of the inductor E_L is

$$E_L = \frac{1}{2} \cdot L \cdot {I_L}^2. \quad (5)$$

The maximum inductor current occurs at a minimum output voltage of 260 V, and the stored energy of the asynchronous algorithm is 68% of that of the conventional algorithm under the same inductance, as shown in Table III. Thus, an inductor core with reduced capacity can be selected for the inductor design, or the core loss of the inductor can be reduced under the same core conditions.

Fig. 8 shows the inductor current ripple calculated by (2) in a half period of the utility. The inductor ripple of the asynchronous algorithm is fixed when the input voltage is higher than the output voltage, because D_{Buck} does not vary at the same voltage condition by (2) and (3). From the asynchronous algorithm, the average inductor ripple is 1.31 A, which is 47% of the value of the conventional algorithm. Thus, the core loss can be reduced under the same inductance condition, or a reduced inductance design can be possible under the same inductor current ripple.

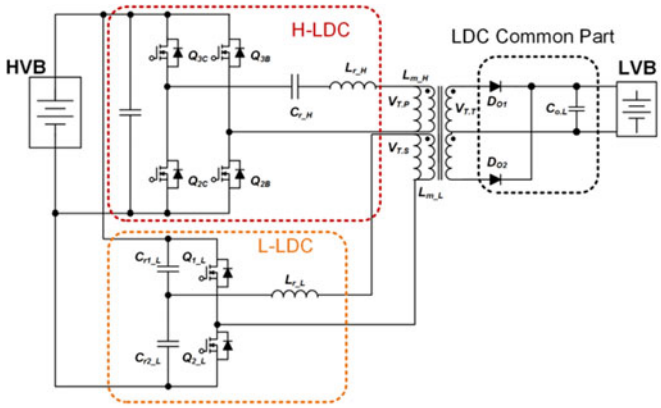

Fig. 9. LDC schemes of the proposed system.

TABLE IV
SPECIFICATIONS OF THE H-LDC AND L-LDC

Parameter		H-LDC	L-LDC
Turn's ratio	$(N_p:N_s)$	26:1	13:1
Resonant capacitor	C_r	34 nF	54 nF
Resonant inductor	L_r	116 μH	58 μH
Magnetizing inductance	L_m	150.8 μH	70 μH
Series resonant frequency	f_r	80.1 kHz	88.3 kHz
Second resonant frequency	f_p	53.8 kHz	59.4 kHz

C. Design and Control Consideration of the LDCs

In consideration of the capacity, the 1.9-kW H-LDC is composed of full-bridge structures that share four MOSFETs of the OBC. The 600-W L-LDC is composed of half-bridge structures by adding two extra MOSFETs because of the simultaneous operation with the OBC, as shown in Fig. 9. And, the L-LDC adopts a split resonant capacitor technique because of its benefit [21]. In designing the LDC, the wide input–output voltage range is a key point in designing the resonant network type. The resonant tank of H-LDC consists of the series resonant capacitor C_{r_L}, the resonant inductor L_{r_L}, and the magnetizing inductor L_m. And, the resonant tank of L-LDC consists of two series resonant capacitors C_{r1_L} and C_{r2_L}, the resonant inductor L_{r_L}, and the magnetizing inductor L_m. The input source of the LDC is the HVB, and the output load is the LVB. Therefore, the LDC has a wide operating range depending on the state of charge of the two batteries.

According to the conventional design process based on the frequency control method [20], [22], the designed LDC parameters are shown in Table IV. The initial turn's ratio of the transformer can be expressed using the nominal operating voltage of the HVB and LVB as

$$n_{\mathrm{H-LDC}} = \frac{V_{\mathrm{HVB.m}}}{V_{\mathrm{LVB.m}}} = \frac{350}{13.5} \approx 26. \tag{6}$$

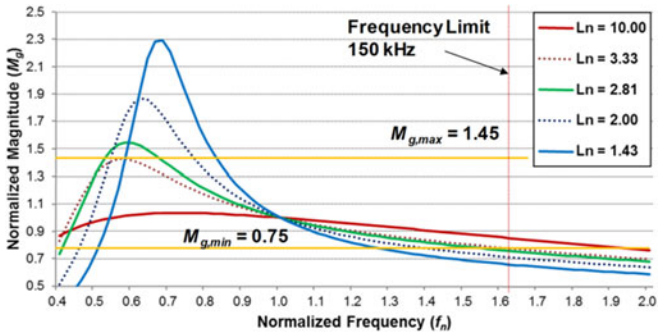

Fig. 10. Voltage gain curve of the H-LDC.

The maximum voltage gain and the minimum voltage gain are given as

$$M_{g.\max} = \frac{n_{\mathrm{H-LDC}} \cdot V_{\mathrm{LVB.max}}}{V_{\mathrm{HVB.min}}} \tag{7}$$

$$M_{g.\min} = \frac{n_{\mathrm{H-LDC}} \cdot V_{\mathrm{LVB.min}}}{V_{\mathrm{HVB.max}}}. \tag{8}$$

In terms of the L-LDC, each parameter can be calculated with same process except that the voltage gain is half because of the half-bridge structure. The series resonant frequency f_r is selected to be 80 kHz by considering EMI characteristics

$$f_r = \frac{1}{2\pi\sqrt{L_r C_r}}. \tag{9}$$

And, the second resonant frequency f_p is [23]

$$f_p = \frac{1}{2\pi\sqrt{(L_r + L_m)C_r}}. \tag{10}$$

Fig. 10 shows the voltage gain curve according to the various inductance ratios L_n. The inductance ratio is given as

$$L_n = \frac{L_m}{L_r} \tag{11}$$

where L_m and L_r are the magnetizing inductance and the leakage inductance, respectively. From the wide voltage gain, the inductance ratio L_n should have a low value by adding an extra inductor or increasing the gap of the transformer. The extra inductor increases the volume and the loss of the system, so it is not a reasonable option. Increasing the gap of the transformer can reduce the inductance ratio L_n, but it can also reduce the efficiency of the system because of the high reluctance of the air gap. Therefore, another approach is needed to overcome these LDC design problems.

D. Proposed LDC Hybrid Control Algorithm

This paper proposes a duty and frequency hybrid control to overcome the problems of the conventional design and control method. The duty control method manages the duty of the switches, unlike the conventional control method. This method can control the output voltage of the *LLC* resonant converter

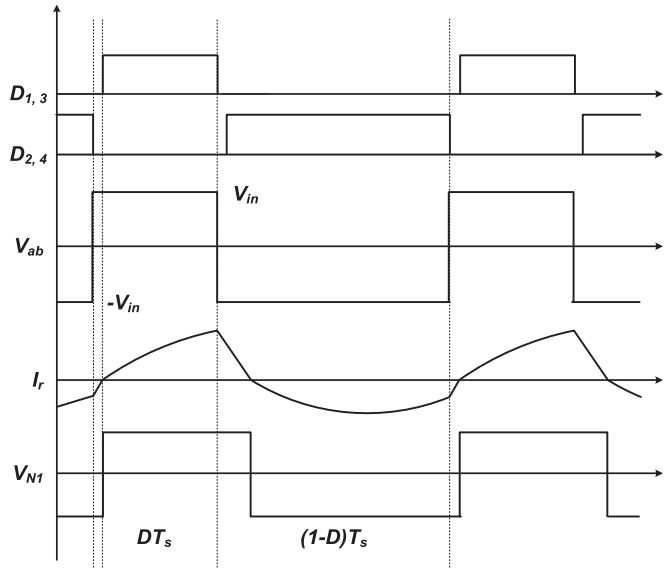

Fig. 11. Steady-state operating waveforms of the duty and frequency control.

by controlling the voltage delivered to the resonant network, as shown in Fig. 11.

The resonant network voltage V_{ab} and the fundamental voltage $V_{ab.1}$ of the *LLC* resonant converter can be expressed as [24]

$$V_{ab} = V_{\text{in}} \cdot (2D-1) + \sum_{h=1}^{\infty} 2\sqrt{2}\left[\frac{V_{\text{in}}}{h\pi} \cdot \sqrt{1-\cos(2\pi hD)} \cdot \sin(h\omega t + \theta_h)\right] \times \left(\theta_h = \tan^{-1}\left[\frac{\sin(2h\pi D)}{1-\cos(2h\pi D)}\right]\right) \quad (12)$$

$$V_{ab.1} = \frac{2\sqrt{2}V_{\text{in}}\sin(\pi D)}{\pi}. \quad (13)$$

The input–output voltage gain of the *LLC* resonant converter can be derived as

$$M_g = \frac{2\sqrt{2}\sin(\pi D)}{\pi\sqrt{1+Q^2\cdot(\omega_n - \frac{1}{\omega_n})^2}} \quad (14)$$

The magnitude of the fundamental has a value of less than 1. The output voltage, therefore, can be controlled by adapting the duty and frequency control method without increasing the gap of the transformer and exceeding the maximum frequency of 150 kHz. However, the rms value of the resonant current is increased, which can cause the saturation of the transformer and increase the conduction losses of the primary-side of the LDC. Thus, the duty control method is adequate for the light-load condition because of its characteristics. Fig. 12 shows the proposed duty and frequency algorithm. The proposed algorithm controls the frequency of the LDC under a 150-kHz switching frequency. When the output voltage cannot be controlled under a 150-kHz switching frequency, the proposed controller fixes the switching frequency at 150 kHz and controls the duty ratio

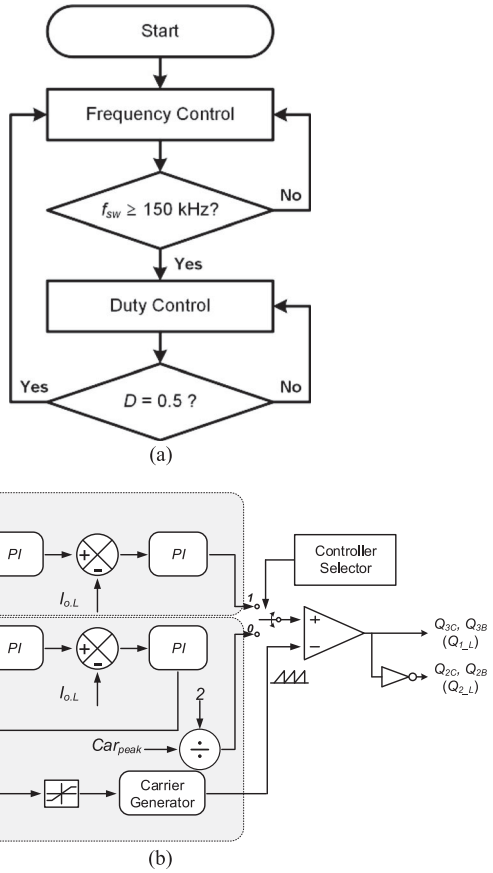

Fig. 12. Proposed frequency and duty control algorithm for LDC: (a) controller select flowchart and (b) control block diagram.

TABLE V
REDESIGNED SPECIFICATIONS OF THE H-LDC AND L-LDC

Parameter		H-LDC	L-LDC
Turn's ratio	$(N_p:N_s)$	20.4:1	10.9:1
Resonant capacitor	C_r	67.2 nF	67.2 nF
Resonant inductor	L_r	53.1 μH	39.8 μH
Magnetizing inductance	L_m	148.9 μH	75.7 μH
Series resonant frequency	f_r	84.3 kHz	97.3 kHz
Second resonant frequency	f_p	43.2 kHz	57.1 kHz

of each switch, as shown in Fig. 12(a). From the proposed controller, the duty control is operated at the light-load condition because of the characteristic of the *LLC* resonant converter. Thus, the aforementioned problems do not occur.

From the proposed algorithm, the minimum voltage gain can be achieved by the increased the inductance ratio, and the transformer turn's ratio can be reduced. The redesigned LDC parameters are shown in Table V. A PM12EQ5050 from Todaisu is selected as the core of the transformer, as shown in Fig. 13. The resonant network is composed of the transformer and resonant capacitor without an extra resonant inductor. The leakage inductance is decreased compared with Table IV, i.e., the air gap of the transformer can be reduced. Thus, the efficiency of the

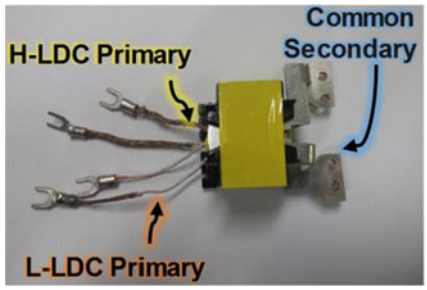

Fig. 13. Designed transformer for H-LDC and L-LDC.

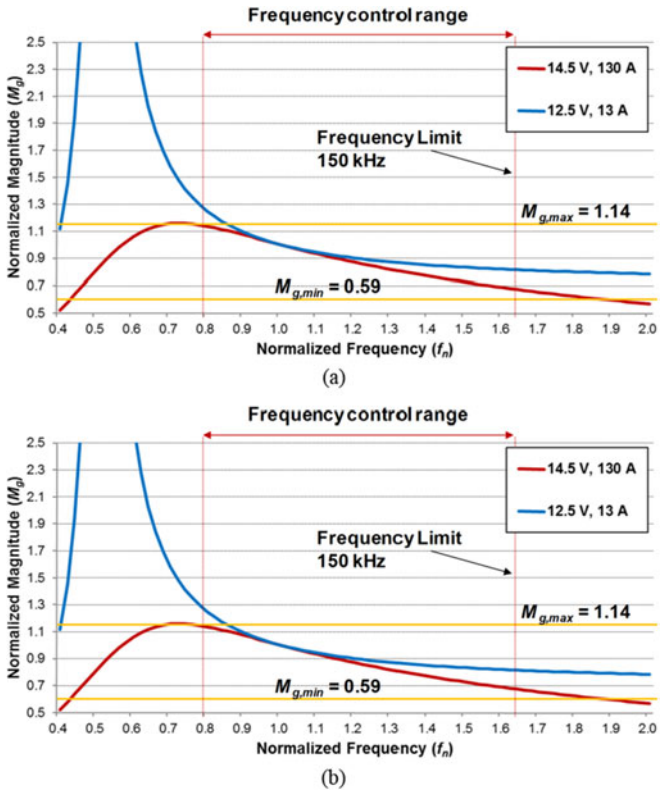

Fig. 14. Input–output gain curves of (a) H-LDC and (b) L-LDC.

transformer is increased. The curves of the input–output voltage gain of the LDCs are shown in Fig. 14. The switching frequency is less than 150 kHz, and the LDC is controlled by the frequency control method. The *LLC* resonant converters are controlled by the duty and frequency control method at 150 kHz to control the output voltage.

IV. Performance Evaluation of the Proposed Battery Charger

To verify the proposed integrated system, experiments were performed using a 6.6-kW prototype, as shown in Fig. 15. The TMS320F28335 digital controller from TI Corp. was used for system control. Table VI lists the specifications in detail.

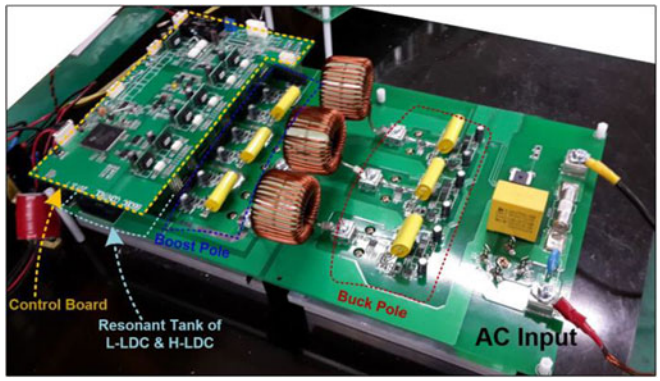

Fig. 15. Prototype of the proposed integrated power unit.

TABLE VI
Specifications of the Proposed System

Parameter	Symbol	Specification	Manufacturer/Part Name
Bridge diode	$D_{R1}-D_{R4}$	600 V/50 A	Fagor/FB5006
OBC switch	$Q_{1A}-Q_{3C}$	650 V/80 mΩ	Infineon/IPW65R080CFDA
OBC buck diode	$D_{1A}-D_{1C}$	650 V/1.7 V	Infineon/IDW20G65C5
L-LDC switch	Q_{1_L}, Q_{2_L}	650 V/110 mΩ	Infineon/IPP65R110CFDA
LDC secondary diode	D_{o1}, D_{o2}	200 V/0.89 V	IXYS/DSEI 2X121
OBC inductor	$I_{L1}-I_{L3}$	400 μH	ChangSung/CH400125
Transformer	T	EQ5050	Todaisu/PM12EQ5050
Controller		150 MHz	TI/TMS320F28335

A. Mode I

The operation of Mode I, where the OBC operates alone, was verified using a rated input voltage of 220 V_{ac} with a 50-kHz switching frequency. Fig. 16 shows the waveforms of the asynchronous algorithm according to the operating mode and the output regulation performance. Fig. 16(a) shows the inductor current according to PWM signals. Each signal is controlled asynchronously, and the buck duty maintains a large duty ratio. When the input voltage is 220 V_{ac}, the OBC operates in step-down mode and step-up mode according to the output voltage. When the output voltage is greater than the peak value of the input voltage, the OBC performs the step-down operation with the asynchronous control algorithm, as shown in Fig. 16(b). In the opposite case, the OBC charges the HVB by boosting the PF correction operation, as shown in Fig. 16(c). The input current and the output voltage are well controlled, and the output voltage is controlled to be stable regardless of the output voltage variations, as shown in Fig. 16(d). Fig. 17 shows graphs of the efficiency and PF. From the asynchronous algorithm, high efficiency (over 97%) can be achieved in step-down mode, and the maximum efficiency is 97.3% in step-up mode operation.

B. Mode II

The operation of Mode II, where the H-LDC operates alone, was verified under the conditions of variable input voltage and output voltage. Fig. 18 shows the experimental results under

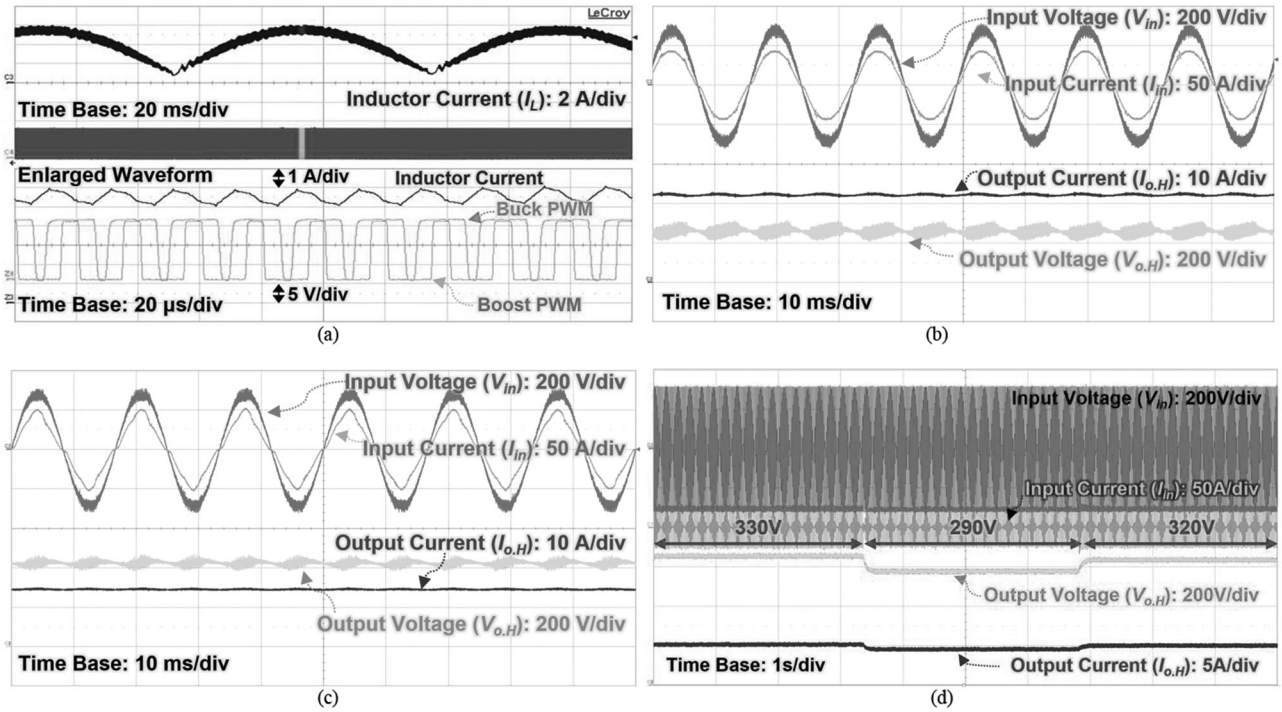

Fig. 16. Waveforms of Mode I: (a) PWM signal and inductor current; (b) $V_{o.H} = 260$ V, $P_{o.H} = 6.6$ kW; (c) $V_{o.H} = 430$ V, $P_{o.H} = 6.6$ kW; and (d) output regulation.

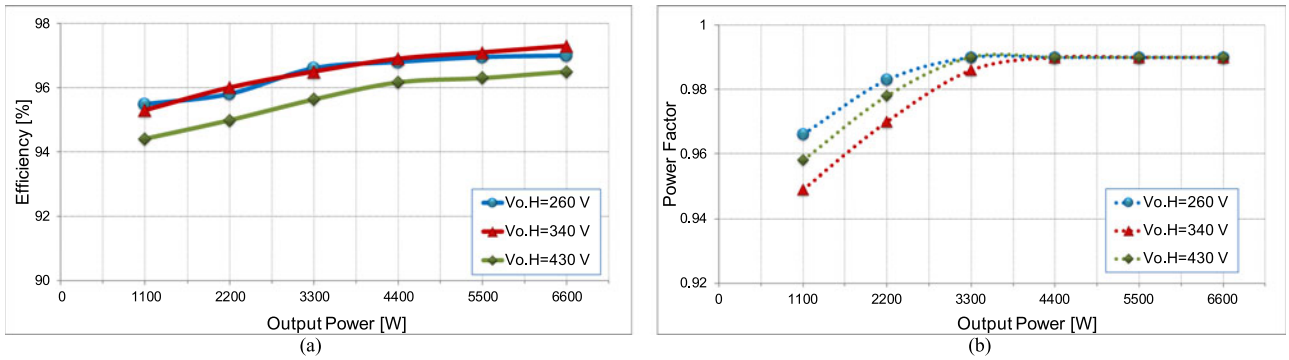

Fig. 17. (a) Efficiency and (b) PF for each input condition.

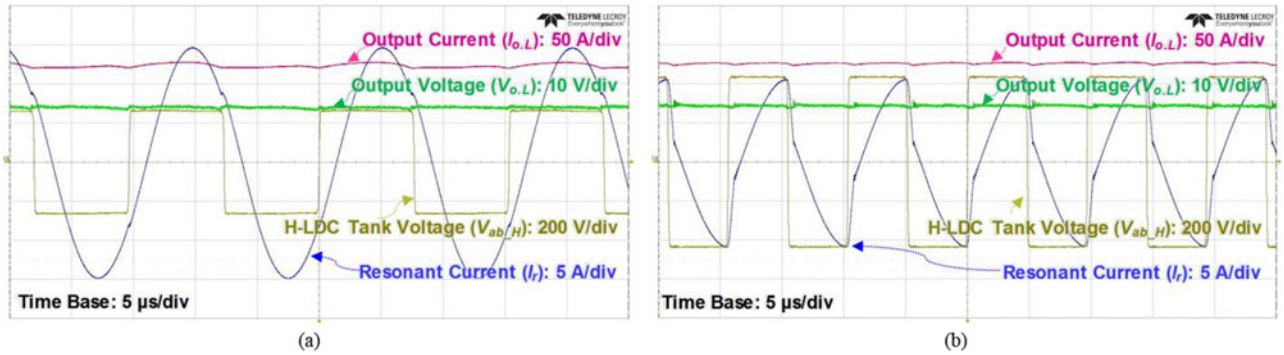

Fig. 18. Waveforms of Mode II operation with frequency control for each voltage gain: (a) $V_{o.H} = 260$ V, $V_{o.L} = 14.5$ V, $I_o = 130$ A, $f_{\rm sw} = 63.7$ kHz; (b) $V_{o.H} = 430$ V, $V_{o.L} = 12.5$ V, $I_o = 130$ A, and $f_{\rm sw} = 103.4$ kHz.

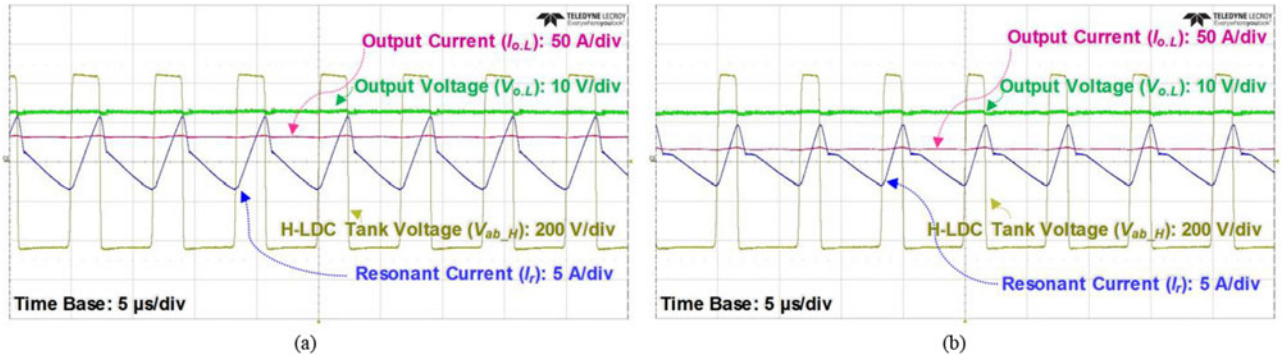

Fig. 19. Waveforms of Mode II operation with duty control for each voltage gain: (a) $V_{o.H} = 430$ V, $V_{o.L} = 12.5$ V, $P_o = 600$ W, $f_{\rm sw} = 150$ kHz; (b) $V_{o.H} = 430$ V, $V_{o.L} = 12.5$ V, $P_o = 400$ W, and $f_{\rm sw} = 150$ kHz.

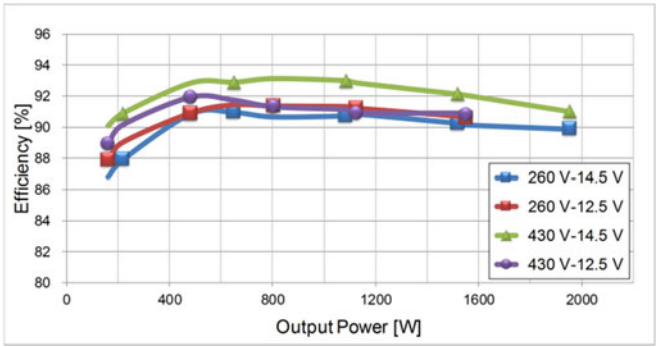

Fig. 20. Efficiency of the H-LDC.

the frequency control operation for the maximum and minimum voltage gain operation at the maximum load condition. To achieve the maximum voltage gain, the switching frequency is 63.7 kHz, which is lower than the designed series resonant frequency f_r and above the second resonant frequency f_p, as shown in Fig. 18(a). The switching frequency is 103.4 kHz for the minimum voltage gain because of the full-load condition. The operating condition where the switching frequency is higher than 150 kHz occurred at a light load and lower voltage gain. In this condition, the H-LDC is operated by the duty control with a fixed frequency of 150 kHz, as shown in Fig. 19. The output voltage is regulated by controlling only the duty variation, and the switches achieve zero-voltage switching (ZVS) turn-on. The duty of Fig. 19(b) is smaller than that of Fig. 19(a) because of the minimum voltage gain. The maximum efficiency of the H-LDC is greater than 93%. When the input voltage is 430 V and the output voltage is 14.5 V, the efficiency is 93.13%, which is the maximum efficiency point, as shown in Fig. 20.

C. Mode III

Mode III is the operating mode where the OBC and L-LDC operate at the same time. The operating characteristic of the L-LDC was identified with the same H-LDC operating conditions. Fig. 21 shows the experimental results of the L-LDC system for the maximum and minimum voltage gain with maximum output current. The switching frequency of Fig. 21(a) is below the series resonant frequency and above the second resonant frequency to achieve the maximum voltage gain. Otherwise, the switching frequency of Fig. 21(b) is above the series resonant frequency. Fig. 22 shows the experimental results for simultaneous operation of the OBC and L-LDC. The nonisolated OBC controls the HVB at 260 V with the asynchronous algorithm, as shown in Fig. 22(a). The L-LDC controls the LVB at 12.5 V, and thus, the L-LDC is operated in the minimum input voltage and the minimum output voltage condition. Because of the high voltage gain, the switching frequency is nearby the series resonant frequency. Fig. 22(b) shows the experimental result that is the maximum input voltage and the maximum output voltage operation condition of the L-LDC. Thus, the nonisolate OBC controls the HVB at 430 V and the L-LDC controls the LVB at 12.5 V. Each operation achieves the input current PF control and ZVS turn-on. Fig. 23 shows the efficiency of the L-LDC. The maximum efficiency is 92.2% when the input voltage is 430 V because of the low conduction loss.

D. Comparative Analysis of Proposed System

In order to evaluate a performance of the proposed integrated charger, a comparative analysis is conducted with the conventional OBC–LDC structure. Fig. 24 shows the schematic of the nonisolated OBC and the LDC without integration. From the cascaded connection between the OBC and the LDC, the LDC can be operated independently from the OBC operation with simple structure. However, additional parts such as switches for the full-bridge structure, gate drivers, heat sink, cooler, and wires, are needed compared with the proposed scheme. Table VII for a comparison between the conventional scheme and the proposed scheme.

In terms of the numbers of components for the proposed system, although two switches and gate drivers are reduced, a relay, resonant capacitors and wires for transformer are added. Thus, the number of components is similar. However, the switch volume is reduced approximately 21% because of a difference switch package type. The volume of the gate driver is also reduced by half, and the gate driver can be designed with a low current capability. Moreover, the primary-side heat sink of

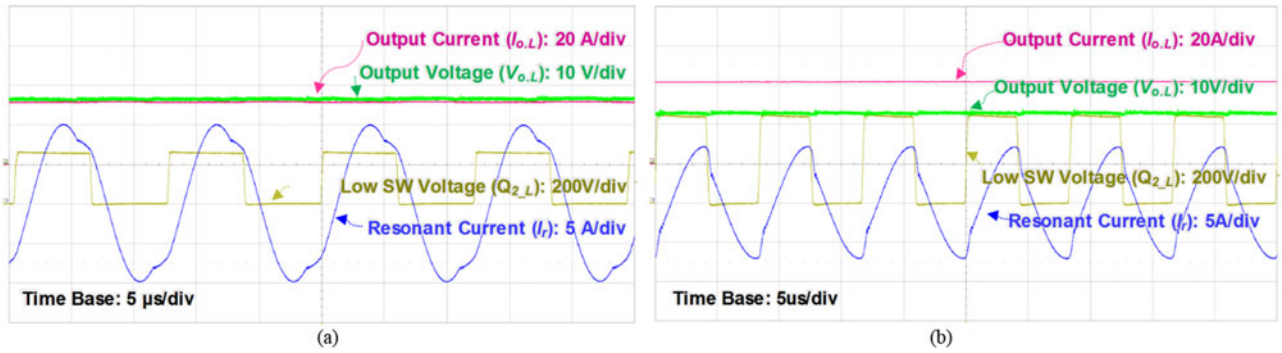

Fig. 21. Waveforms of Mode III operation for each voltage gain: (a) $V_{o.H} = 260$ V, $V_{o.L} = 14.5$ V, $P_o = 600$ W, $f_{\rm sw} = 70$ kHz; (b) $V_{o.H} = 430$ V, $V_{o.L} = 12.5$ V, $P_o = 600$ W, and $f_{\rm sw} = 120$ kHz.

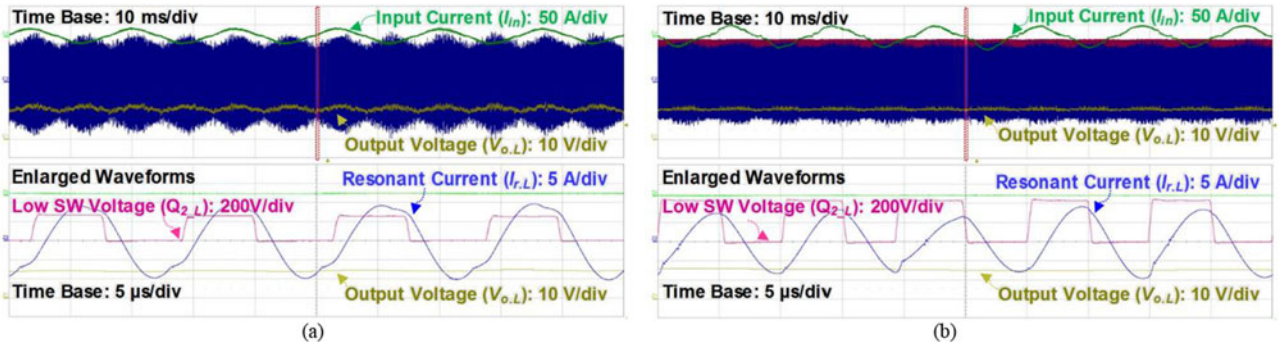

Fig. 22. Simultaneous waveforms of Mode III operation for each voltage gain: (a) $P_{\rm OBC} = 2.8$ kW, $P_{\rm L-LDC} = 500$ W; (b) $P_{\rm OBC} = 4$ kW, and $P_{\rm L-LDC} = 600$ W.

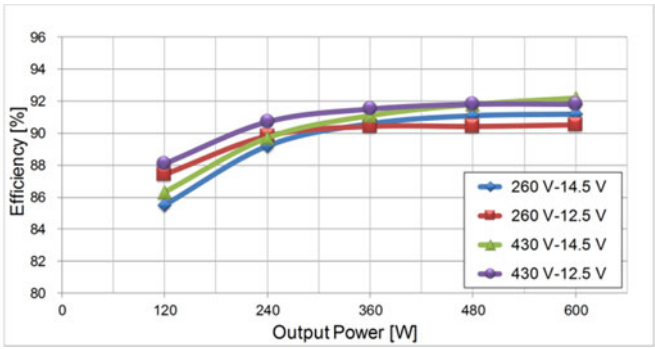

Fig. 23. Efficiency of the H-LDC.

the LDC is reduced dramatically, because the power rating is decreased from 1.9-kW to 600 W. Fig. 25 shows a comparison of each component volume based on components of Table VI. The total component volume reduction is 367.3 cm^3. And, in the conventional LDC, the high-power cable between the HVB and the LDC should be used. However, in the proposed system, it can be eliminated. From the component volume reduction and power cable eliminated, the total volume of LDC is 1.87 L. An average LDC volume of reported research and products is approximately 2.2 L. Thus, the power density can be increased by adopting the proposed system.

Fig. 26 shows the efficiency comparison between the LDC of the proposed system and LDCs of the conventional structure nearby 1.9-kW power rate [25]–[27]. In this comparison, the proposed integrated battery charger shows similar efficiency results in spite of increased power density.

V. Conclusion

In this paper, the design and implementation of an integrated power unit for EVs was presented in order to improve the power density and efficiency. An integrated charger structure to integrate the OBC and LDC was proposed by using a structural analysis of a cascaded buck–boost converter. The design method for the OBC and an asynchronous control algorithm to reduce the inductor current were proposed. The integration of the LDC, which shares the transformer and the second side, with a duty and frequency control to improve efficiency, was designed. The proposed integrated power unit minimizes both the number of power devices and the volume of the passive components. In addition, efficiency was improved by adapting novel control algorithms such as an asynchronous control algorithm for the OBC and a duty and frequency hybrid control algorithm for the LDC. High performance in charging the batteries was also achieved across a wide input and output voltage range. The proposed integrated power unit including control algorithm was verified by experiment under various operation conditions. The OBC prototype achieves a peak efficiency value of 97.3% in boost operation mode and 97% in buck operation mode. The H-LDC achieves a peak efficiency of 93.1%, and the L-LDC

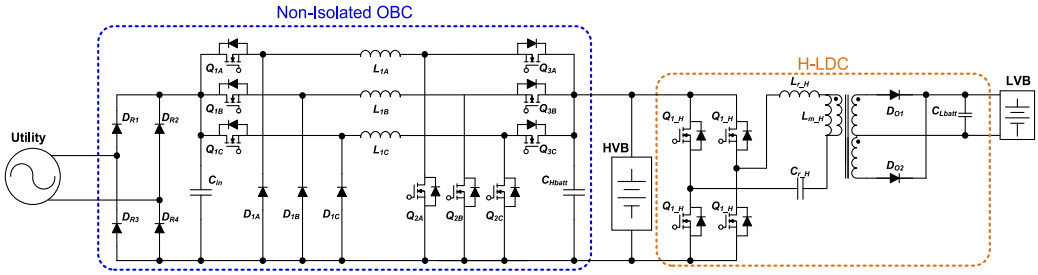

Fig. 24. Nonisolated OBC with cascaded connection LDC.

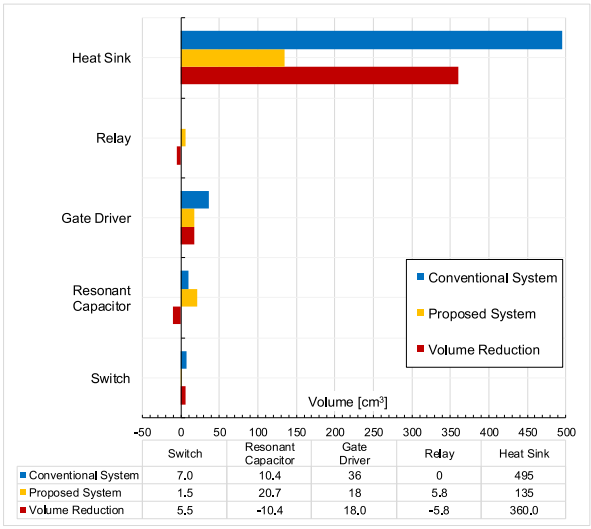

	Switch	Resonant Capacitor	Gate Driver	Relay	Heat Sink
Conventional System	7.0	10.4	36	0	495
Proposed System	1.5	20.7	18	5.8	135
Volume Reduction	5.5	-10.4	18.0	-5.8	360.0

Fig. 25. Comparison of additional component volume of LDC between conventional and proposed systems.

TABLE VII
COMPARISON OF ADDITIONAL COMPONENTS FOR LDC BETWEEN CONVENTIONAL AND PROPOSED SYSTEMS

Additional Component	Conventional LDC (see Fig. 24)	Proposed	
		H-LDC	L-LDC
Switch	4 (TO-247)	0	2 (TO-220)
Gate driver	4	0	2
Heat sink	Require	Not require	Require
Resonant capacitor	Require	Require	Require
Wire for transformer	Require	Require	Require
Power and signal cable	Require	Not require	Require
Relay	0	1	0

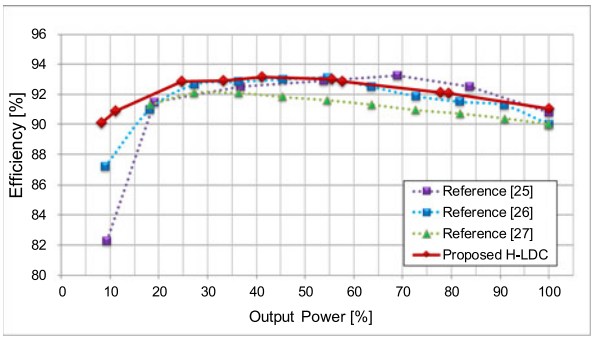

Fig. 26. Comparison of H-LDC efficiency between conventional and proposed systems.

achieves a peak efficiency of 92.2%. And, the total volume of the LDCs is 1.87L, which is 85% of the conventional LDC average volume, by maintaining the efficiency compared with other research. Therefore, the proposed integrated system could be used as an effective method for increasing power density of PCUs for EVs.

REFERENCES

[1] P. Crist, "Electric Vehicles Revisited Costs, Subsidies and Prospects," *Int. Trans. Forum, Paris, Tech. Rep.*, 2012. [Online]. Available: http://www.internationaltransportforum.org/jtrc/DiscussionPapers/DP201203.pdf

[2] S. Nozawa, T. Maekawa, E. Yagi, Y. Terao, and H. Kohno, "Development of new power control unit for compact-class vehicle," in *Proc. Int. Symp. Power Semicond. Devices IC's*, 2010, pp. 43–45.

[3] S. H. Kim and K. F. Soon, "Multifunctional onboard battery charger for plug-in electric vehicles," *IEEE Trans. Ind. Electron*, vol. 62, no. 6, pp. 3460–3472, Jun. 2015.

[4] Y. S. Kim, C. Y. Oh, W. Y. Sung, B. K. Lee, and G. C. Park, "Optimal design and control of OBC–LDC integrated power unit for electric vehicles," in *Proc. IEEE Appl. Power Electron. Conf. Expo.*, Fort Worth, TX, USA, 2014, pp. 3192–3198.

[5] D. Ouwerkerk, T. Han, and J. Preston, "Efficiency improvement using a hybrid power module in 6.6 kW non-isolated on-vehicle charger," in *Proc. IEEE Veh. Power Propul. Conf.*, Seoul, Korea, 2012, pp. 284–288.

[6] C. Y. Oh, D. H. Kim, D. G. Woo, W. Y. Sung, Y. S. Kim, and B. K. Lee, "A high-efficient nonisolated single-stage on-board battery charger for electric vehicles," *IEEE Trans. Power Electron.*, vol. 28, no. 12, pp. 5746–5757, Dec. 2013.

[7] M. Yilmaz and P. T. Krein, "Review of battery charger topologies, charging power levels, and infrastructure for plug-in electric and hybrid vehicles," *IEEE Trans. Power Electron.*, vol. 28, no. 5, pp. 2151–2169, May 2013.

[8] D. H. Kim, M. J. Kim, S. H. Ryu, Y. S. Kim, and B. K. Lee, "Asymmetric control algorithm non-isolated type on-board battery charger with single controller," in *Proc. IEEE Applied Power Electron. Conf. Expo.*, Fort Worth, TX, USA, 2014, pp. 3199–3204.

[9] A. Albanna, M. N. Arafat, A. Gupta, M Anwar, and M. Teimor, "Analysis of ground fault currents in isolated and non-isolated charging modules in electric vehicles," in *Proc. IEEE Trans. Electrific. Conf. Expo.*, Dearborn, MI, USA, 2015, pp. 1–6.

[10] *Electric Vehicle and Plug in Hybrid Electric Vehicle Conductive Charger Coupler*, SAE International, Standard Recommended Practice J1772, Jan. 2010.

[11] L. Solero, "Nonconventional on-board charger for electric vehicle propulsion batteries," *IEEE Trans. Veh. Technol.*, vol. 50, no. 1, pp. 144–149, Jan. 2001.

[12] Y. Hu. X. Song, W. Cao, and B. Ji, "New SR drive with integrated charging capacity for plug-in hybrid electric vehicles (PHEVs)," *IEEE Trans. Ind. Electron.*, vol. 61, no. 10, pp. 5722–5731, Oct. 2014.

[13] S. Haghbin, S. Lundmark, M. Alaküla, and O. Carlson, "Grid-connected integrated battery chargers in vehicle applications: Review and new solution," *IEEE Trans. Ind. Electron.*, vol. 60, no. 2, pp. 459–473, Feb. 2013.

[14] G. Pellegrino, E. Armando, and P. Guglielmi, "An integral battery charger with power factor correction for electric scooter," *IEEE Trans. Power Electron.*, vol. 25, no. 3, pp. 751–759, Mar. 2010.

[15] O. Hegazy, R. Barrero, J. V. Mierlo, P. Lataire, N. Omar, and T. Coosemans, "An advanced power electronics interface for electric vehicles applications," *IEEE Trans. Power Electron.*, vol. 28, no. 12, pp. 5508–5521, Dec. 2013.
[16] S. Haghibin, K. Khan, S. Zhao, M. Alakula, S. Lundmark, and O. Carlson, "An integrated 20-kW motor drive and isolated battery charger for plug-in vehicles," *IEEE Trans. Power Electron.*, vol. 28, no. 8, pp. 4013–4029, Aug. 2013.
[17] S. Lacroix, E. Laboure, and M. Hilairet, "An integrated fast battery charger for electric vehicle," in *Proc. IEEE Veh. Power Propul. Conf.*, Lille, France, 2010, pp. 1–6.
[18] S. Dusmez and A. Khaligh, "A charge-nonlinear-carrier-controlled reduced-part single-stage integrated power electronics interface for automotive applications," *IEEE Trans. Veh. Technol*, vol. 63, no. 3, pp. 1091–1103, Mar. 2014.
[19] J. C. Kim, "Development of low voltage DC–DC converter for electrical equipment in hybrid electric vehicle," in *Proc. Korean Soc. Autom. Eng. Electr. Drive Veh. Division Workshop*, Jul. 2012, pp. 222–232.
[20] H. Huang, "Designing an LLC resonant half-bridge power converter," in *Proc. Texas Instrum. Power Supply Seminar*, 2010, pp. 1–27.
[21] F. D. Domenico, A. Steiner, and J. Catly, "Design of a 600 W HB LLC converter using 600 V CoolMOS^{TM} P6," *Appl. Note, Infineon*, Munich, Germany, Jul. 2015.
[22] R. L. Steigerwald, "A comparison of half-bridge resonant converter topologies," *IEEE Trans. Power Electron.*, vol. 3, no. 2, pp. 174–182, Apr. 1988.
[23] J. Deng, S. Li, S. Hu, C. C. Mi, and R. Ma, "Design methodology of LLC resonant converters for electric vehicle battery chargers," *IEEE Trans. Veh. Technol.*, vol. 63, no. 4, pp. 1581–1592, May 2014.
[24] S. H. Ryu, D. H. Kim, M. J. Kim, J. S. Kim, and B. K. Lee, "Adjustable frequency–duty-cycle hybrid control strategy for full-bridge series resonant converters in electric vehicle chargers," *IEEE Trans. Ind. Electron*, vol. 61, no. 10, pp. 5354–5362, Oct. 2014.
[25] D. W. Lee, "Introduction on xEV automotive AC/DC, DC/DC solution and CoolMOSTM CFDA," *Infineon Webinar*, 2014. [Online]. Available: https://www.eewebinar.co.kr/techNote_dn.asp?idx=181
[26] Y. S. Kim, C. Y. Oh, W. Y. Sung, and B. K Lee, "Topology and control scheme of OBC–LDC integrated power unit for electric vehicles," *IEEE Trans. Power Electron.*, to be published.
[27] Y. S. Kim, D. W. Jung, and B. K. Lee, "Advanced LDC test bed using energy recovery technique for HEVs," *J. Electr. Eng. Technol.*, vol. 8, no. 4, pp. 911–919, Aug. 2013.

Dong-Hee Kim (S'10–M'15) received the B.S., M.S., and Ph.D. degrees from Sungkyunkwan University, Suwon, Korea, in 2009, 2011, and 2015, respectively, all in electrical engineering.

From 2015 to 2016, he was a Postdoc Researcher in Sunkyunkwan University. In 2016, he was a Part-Time Lecturer at Daejin University, Korea, and Shandong University of Technology, China. In 2016, he joined the Department of Electrical Engineering, Tongmyung University, Busan, Korea, as an Assistant Professor. His current research interests include power conditioning system and dc–dc converter for renewable energy and battery charger for hybrid electric vehicles/electric vehicles.

Min-Jung Kim (S'13) received the B.S. degrees, in 2012, from Sungkyunkwan University, Suwon, Korea, where he is currently working toward the master's/Ph.D. degree in electrical engineering.

His current research interest includes battery charger for HEVs/EV.

Byoung-Kuk Lee (S'97–M'02–SM'04) received the B.S. and the M.S. degrees from Hanyang University, Seoul, Korea, in 1994 and 1996, respectively, and the Ph.D. degree from Texas A&M University, College Station, TX, USA, in 2001, all in electrical engineering.

From 2003 to 2005, he was a Senior Researcher at Power Electronics Group, Korea Electrotechnology Research Institute (KERI), Changwon, Korea. In 2006, he joined the College of Information and Communication Engineering, Sungkyunkwan University, Suwon, Korea. His current research interests include on-board chargers and wireless power transfer chargers for electric vehicles, BMS algorithms, energy storage systems, hybrid renewable energy systems, dc distribution systems for home appliances, modeling and simulation, and power electronics.

Prof. Lee is a Recipient of the Outstanding Scientists of the 21st Century from IBC and listed on 2008 Ed. of Who's Who in America and 2009 Ed. of Who's Who in the World. He is a Guest Associate Editor for the IEEE TRANSACTIONS ON POWER ELECTRONICS and the Associate Editor for the IEEE TRANSACTIONS ON TRANSPORTATION ELECTRIFICATION. He was the Presenter for Professional Education Seminar with the topic of "On-Board Charger Technology for EVs and PHEVs" at the IEEE Applied Power Electronics Conference in 2014. He was the General Chair for the IEEE Vehicular Power and Propulsion Conference (VPPC) in 2012 and is a Member of the IEC Conformity Assessment Board (CAB) from 2016.